

The Effect of the Horizontal Component of the Angular Velocity of the Earth's Rotation on Inertia-Gravity Waves

Yuki YASUDA

and

Kaoru SATO

Department of Earth and Planetary Science, The University of Tokyo, Tokyo, Japan

(Manuscript received 27 February 2012, in final form 12 October 2012)

Abstract

By using a linearized Boussinesq model on the tangent plane in the mid-latitudes, how the effect of the horizontal component of the angular velocity of the Earth's rotation (f_H -effect) modifies the characteristics of inertia-gravity waves is examined. The f_H -effect widens the range of the intrinsic wave frequency. A physical interpretation of this modification is made in terms of restoring forces. There are cases in which the rotational direction of the hodograph with time is anticlockwise (clockwise) even in the Northern (Southern) Hemisphere, unlike the case of $f_H = 0$. Considering the form stress over the potential temperature surface, the sign of the vertical group velocity can be the same as that of the vertical phase speed, unlike the case of $f_H = 0$, because the f_H -effect can reverse the direction of the form stress through the vertical force balance. The minimum frequency increases with the buoyancy frequency (N) for $f_H \neq 0$, when the latitude and the direction of the wavevector are fixed. This fact indicates that waves trapped in a weakly stratified layer (WSL) exist, where N is low. Using an idealized vertical profile of N in the form of a square well, the trapped wave solution is derived. The solution is composed of two plane waves in the WSL, while it decays exponentially outside. Using operational radiosonde data in Japan, it is shown that there is a persistent WSL slightly below the tropopause where the climatological minimum value of N (N_{\min}) is about a half times lower than the typical tropospheric value ($\sim 0.01 \text{ s}^{-1}$). The N_{\min} value is not sufficiently small to form trapped waves having wavelengths in a realistic range within a few days, because the condition of $N_{\min} < 0.001 \text{ s}^{-1}$ is necessary. Thus, such trapped waves are rarely observed in the WSL slightly below the tropopause.

Keywords inertia-gravity wave; traditional approximation; angular velocity of the Earth's rotation; tropopause; hodograph; form stress

1. Introduction

In many geophysical problems, only a component of the Coriolis force that is proportional to the Coriolis parameter f_v ($\equiv 2\Omega \sin \phi$) is considered, where Ω is the magnitude of the angular velocity of the Earth's rotation and ϕ is the latitude. In this paper, we call

this manipulation the traditional approximation (TA). The TA is equivalent to the assumption that the angular velocity of the Earth's rotation is locally vertical, since f_v is proportional to the vertical component of Ω . When the hydrostatic balance or shallow approximation is used in the equations of motion, the TA needs to be used to satisfy the conservation laws of energy, potential vorticity, and angular momentum (Holton 2004; White et al. 2005). In this paper, we discuss the effect of another component of the Coriolis force proportional to f_H ($\equiv 2\Omega \cos \phi$), which is two times as large as the horizontal component of Ω . Hereafter, the

Corresponding author: Yuki Yasuda, Department of Earth & Planetary Science, The University of Tokyo, 7-3-1, Hongo, Bunkyo-Ku, Tokyo 113-0033, Japan.
E-mail: yyuuki@eps.s.u-tokyo.ac.jp
©2013, Meteorological Society of Japan

terms proportional to f_H (f_i) are referred to as the f_H -terms (f_i -terms).

In the 1970s, several studies were reported on the effects of f_H -terms (f_H -effect). By using a linearized Boussinesq model in the ocean, Saint-Guilly (1970) showed that the range of internal wave frequency is enlarged and that there are waves vertically trapped in the pycnocline due to the tilt of Ω from the vertical.

Recently, the f_H -effect has been revisited for the development of high-resolution weather prediction models of atmosphere and ocean including small-scale phenomena. Thuburn et al. (2002) and Kasahara (2003) analytically examined wave modes in the ocean bounded vertically at the top and bottom with Cartesian coordinates on the tangent plane. They obtained a solution of a new wave mode, which exists because of the f_H -effect, in addition to well-known solutions of two modes, acoustic mode and inertia-gravity mode, which are slightly modified by the f_H -effect. It was shown that this new mode is identical to the mode obtained by Saint-Guilly (1970). This new mode is called the sub-inertial mode, while the traditional inertia-gravity mode is called the super-inertial mode. The wave frequencies of the former are slightly lower than the inertial frequency (Coriolis parameter) f_i , while those of the latter are higher than f_i . The sub-inertial mode is mainly present in the weakly stratified layer (WSL) where the buoyancy frequency N is low, while the super-inertial mode is mainly present in the strongly stratified layer (SSL) (Gerkema and Shrira 2005a; Kasahara and Gary 2006). The reason for the sub-inertial mode presence is that the f_H -effect is related to vertical motion, which is large in the WSL. At first sight, the sub-inertial mode looks different from the super-inertial mode.

More precise interpretation was given by Durran and Bretherton (2004): The sub- and super-inertial modes are simply the superposition of two plane waves. When $f_H = 0$, to satisfy the boundary condition that the vertical velocity is zero at top and bottom boundaries, there is one way of superposing two plane waves with frequencies higher than f_i , which, respectively, propagate energy upward and downward. On the other hand, when $f_H \neq 0$, there is another possible way of superposing waves with frequencies lower than f_i . The reason for the latter is that the f_H -terms modify the dispersion relation of the plane wave. In this paper, the modification of the dispersion relation is discussed by examining the vertical group velocity c_{gz} in terms of the form stress.

Unlike in the ocean, there is no upper boundary in the atmosphere. This fact means that atmospheric

waves are usually not “modes” that are formed between the two boundaries. Thus, it is valuable to examine the f_H -effect on atmospheric waves. In this paper, it is shown that the sub-inertial waves vertically trapped in the WSL can exist. According to Durran and Bretherton (2004), the necessary condition for the existence of the sub-inertial modes in the vertically bounded domain is that the frequency takes the minimum ω_{\min} at a finite vertical wavenumber. However, this condition is not sufficient for the existence of trapped waves in the WSL. As shown later, it is also necessary that ω_{\min} is a monotonically increasing function of N . For the ocean, Gerkema and Shrira (2005a) briefly noted the possibility of similar sub-inertial waves vertically trapped in the WSL between the seasonal thermocline and the permanent pycnocline. However, existence of the trapped wave solution in the vertically unbounded domain has not been exactly shown. Thus, it is meaningful to examine the f_H -effect in the WSL. The purpose of this study is to examine the f_H -effect on the inertia-gravity waves in the atmosphere.

In Section 2, plane wave solutions in a linearized Boussinesq model containing the f_H -terms on the mid-latitudes tangent plane are examined. In particular, the modifications to the dispersion relation and the hodograph by the f_H -effect are discussed in terms of the force balance. It is shown that taking opposite signs of the vertical group velocity c_{gz} and vertical phase speed c_{pz} is a general wave characteristic for internal plane waves and equatorial waves in the linearized Boussinesq and primitive equations for $f_H = 0$. Furthermore, how this characteristic is modified by the f_H -effect is examined. In Section 3, analytic solutions trapped in the WSL are examined for an idealized distribution of N having the form of a square well. In Section 4, by using radiosonde data in Japan, the structure of N in the meridional cross section is shown. Using the climatological minimum value of N , the f_H -effect on inertia-gravity waves in the real atmosphere is examined. Summary and concluding remarks are discussed in Section 5.

2. Characteristics of plane wave solutions in the linearized Boussinesq model with $f_H \neq 0$

2.1 Formulation and plane wave solutions

In the Cartesian coordinates (x, y, z) with x, y , and z directed eastward, northward and upward, respectively, the components (k, l, m) of the wavevector \mathbf{k} of a plane wave solution are expressed as

$$(k, l, m) = (\kappa \cos \beta \cos \alpha, \kappa \cos \beta \sin \alpha, \kappa \sin \beta), \quad (2.1)$$

where κ is the magnitude of \mathbf{k} , and α and β are the angles of \mathbf{k} from the x axis and the horizontal plane, respectively (Fig. 1). The xyz coordinates are rotated by the angle α around the z axis so as to let a new x axis point to the horizontal wavevector \mathbf{k}_H . These coordinates are referred to as $x'y'z$ coordinates. In the $x'y'z$ coordinates, the equations of the linearized Boussinesq model containing the f_H -terms for the plane wave solution are expressed in the following (Gerkema and Exarchou 2008).

$$\frac{\partial \tilde{u}}{\partial t} - f_V \tilde{v} + f_H \cos \alpha \, w + \frac{1}{\rho_0} \frac{\partial p}{\partial x'} = 0, \quad (2.2a)$$

$$\frac{\partial \tilde{v}}{\partial t} + f_V \tilde{u} - f_H \sin \alpha \, w = 0, \quad (2.2b)$$

$$\frac{\partial w}{\partial t} - f_H \cos \alpha \, \tilde{u} + f_H \sin \alpha \, \tilde{v} - b + \frac{1}{\rho_0} \frac{\partial p}{\partial z} = 0, \quad (2.2c)$$

$$\frac{\partial \tilde{u}}{\partial x'} + \frac{\partial w}{\partial z} = 0, \quad (2.2d)$$

$$\frac{\partial b}{\partial t} + N^2(z)w = 0. \quad (2.2e)$$

Here a motionless and stably stratified basic state is considered. The dependent variables are the velocity components (\tilde{u} , \tilde{v} , w) in (x' , y' , z) together with p and b , which are the perturbation pressure and the buoyancy ($b \equiv g\theta/\theta_0$), respectively, where θ is the perturbation potential temperature from the basic state θ_0 , and $\bar{\theta}_0$ is an average of θ_0 . The constant basic density is ρ_0 . The square of the buoyancy frequency is defined as $N^2 \equiv \frac{g}{\bar{\theta}_0} \frac{d\bar{\theta}_0}{dz}$. To focus on the f_H -effect, the latitudinal gradient of f_V is ignored. In this paper, the case of $N > f_V > 0$ is considered, which is usually valid for the real atmosphere in the mid-latitudes in the Northern Hemisphere. Note that similar theories shown below can be derived for the Southern Hemisphere.

In the $x'y'z$ coordinates, \mathbf{k} is expressed as

$$(\tilde{k}, 0, m) = (\kappa \cos \beta, 0, \kappa \sin \beta), \quad (2.3)$$

where $\tilde{k} (> 0)$ is the x' component of \mathbf{k} . The fluctuation components (\tilde{u} , \tilde{v} , w , b , p) are expressed as

$$(\tilde{u}, \tilde{v}, w, b, p) = (\tilde{u}_0, \tilde{v}_0, w_0, b_0, p_0) \exp i(\tilde{k}x' + mz - \omega t), \quad (2.4)$$

where subscripts 0 denote constant complex numbers. The frequency ω is taken to be positive without losing generality.¹ By considering a constant buoyancy frequency ($N(z) = N_0 (= \text{const})$) and substituting (2.4) into (2.2a)–(2.2e), the dispersion relation is obtained:

$$\omega^2 = \frac{\tilde{k}^2 N_0^2 + (\tilde{k} f_H \sin \alpha + m f_V)^2}{\tilde{k}^2 + m^2} = \frac{(k^2 + l^2) N_0^2 + (l f_H + m f_V)^2}{k^2 + l^2 + m^2}. \quad (2.5)$$

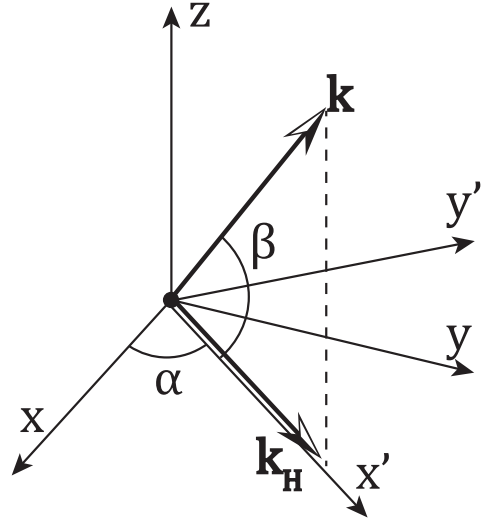


Fig. 1. Positional relation among wavevector \mathbf{k} , xyz coordinates, and $x'y'z$ coordinates. α and β are the angles of \mathbf{k} from the x axis and the horizontal plane, respectively. The x' axis points to the direction of horizontal wavevector \mathbf{k}_H .

The right-hand side of (2.5) is the expression in the xyz coordinates.

Figure 2a shows dispersion curves, i.e., ω as a function of m normalized by \tilde{k} for $f_H = 0$ (a long dashed curve) and $f_H \neq 0$ (a solid curve). Here we take $\alpha = \pi/2$, $\phi = 45^\circ$, and $N_0 = 1.5 f_V$ as an example. It is seen that while $\omega_{\min} = f_V$ and $\omega_{\max} = N_0$ for $f_H = 0$, the range of ω is wider and ω does not show symmetry around $m = 0$ for $f_H \neq 0$. The inclination of the dispersion curve for $f_H = 0$ indicates that the vertical group velocity c_{gz} ($\equiv \partial \omega / \partial m$) is positive (negative) for $m < 0$ ($m > 0$) and zero for $m = 0$. For $f_H \neq 0$, the dispersion curve is modified so that c_{gz} is negative when $m < m_{\min} < 0$ and positive when $0 \leq m < m_{\max}$, respectively, where m_{\min} and m_{\max} are defined as $\omega(m_{\min}) = \omega_{\min}$ and $\omega(m_{\max}) = \omega_{\max}$ for a given α . In other words, the energy propagation is not always upward (downward) when the phase propagation is downward (upward) for $f_H \neq 0$. These features are always seen when $0 < \alpha < \pi$. Here, although we considered an unusual situation of the ratio of f_V and N_0 to clarify the modification by the f_H -effect, similar nature is observed even when $N_0 \gg f_H, f_V$ as in the real atmosphere.

Figure 2b shows dispersion curves for $\alpha = \pm \pi/2$,

¹This generality arises from the fact that the equations of the Boussinesq model have space-inversion and time-reversal symmetries.

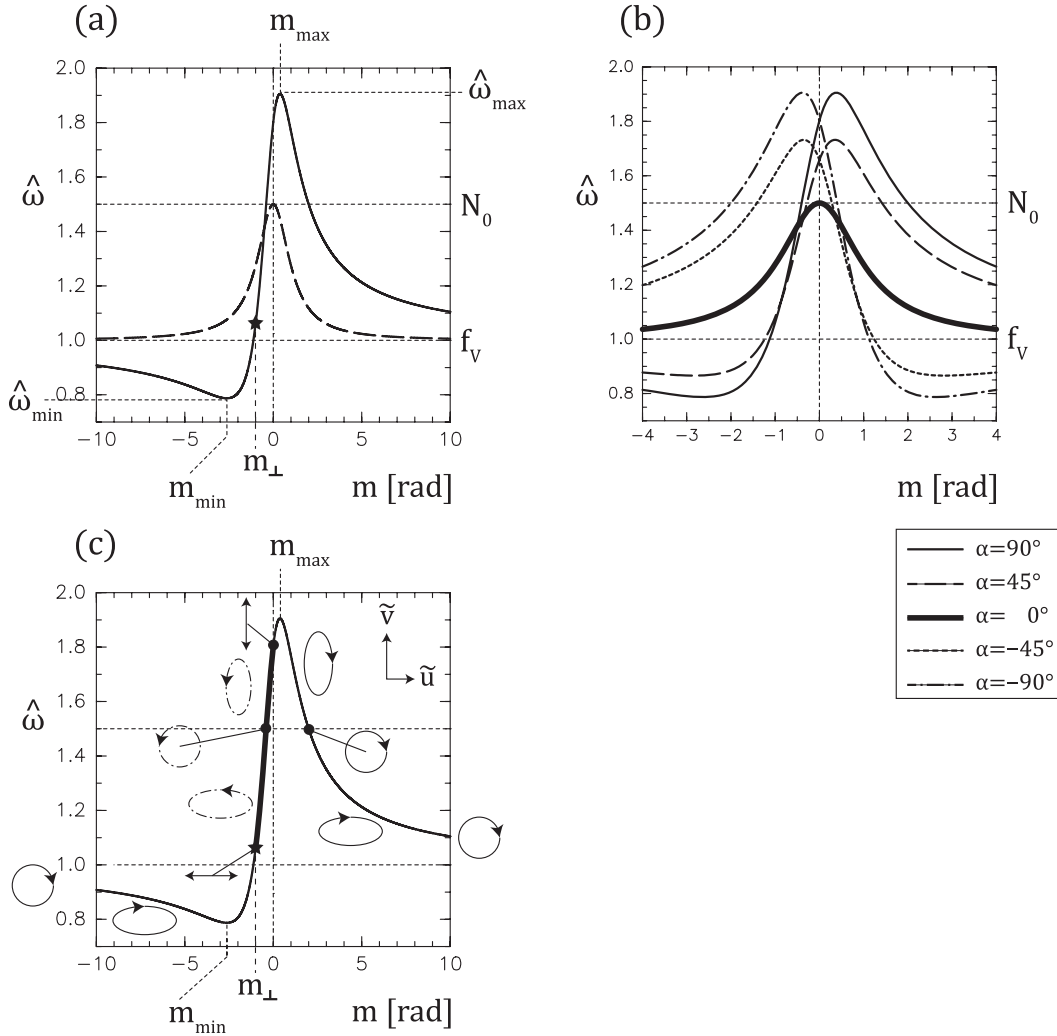


Fig. 2. Frequency $\hat{\omega}$ normalized by f_v as a function of the vertical wave number m normalized by \tilde{k} (a) for $f_H = 0$ and $\alpha = \pi/2$ (a long dashed curve) and for $f_H \neq 0$ and $\alpha = \pi/2$ (a solid curve), and (b) for $f_H \neq 0$ and $\alpha = \pm\pi/2, \pm\pi/4$, and 0 . (c) Hodographs of horizontal wind fluctuations with time for $f_H = 0$ in the $\tilde{u}\tilde{v}$ plane. In (a) and (c), stars on solid curves denote the positions of m_\perp for which \mathbf{k} is perpendicular to $\mathbf{\Omega}$. In (c), a thick part on the solid curve shows the part where the hodograph rotates anticlockwise. $\phi = 45^\circ$ and $N_0 = 1.5 f_v$ are taken.

$\pm\pi/4$, and 0 with $N_0 = 1.5 f_v$. It is seen that when either $\pi < \alpha < 2\pi$ or $f_v < 0$ (i.e., in the Southern Hemisphere), the dispersion curve for $f_H \neq 0$ takes a reflected shape about $m = 0$. When either $\alpha = 0$ or $\alpha = \pi$ (i.e., \mathbf{k}_H points purely eastward or westward), the dispersion curve for $f_H \neq 0$ accords with that for $f_H = 0$. The f_H -effect does not modify the wave characteristics in this case because the effect appears in the form of $f_H \sin \alpha$ in (2.5). The range of $\hat{\omega}$ is the most wide for $\alpha = \pm\pi/2$ (Fig. 2b) for the same horizontal wave number.

2.2 Intuitive interpretation on the modification of the maximum and minimum of $\hat{\omega}$ by the f_H -effect

Gerkema and Exarchou (2008) mathematically showed that the range of $\hat{\omega}$ becomes wider for $f_H \neq 0$. However, its physical explanation has not been clarified yet. In this subsection, the modifications to the maximum and minimum frequencies ($\hat{\omega}_{\max}$ and $\hat{\omega}_{\min}$) by the f_H -effect are examined from the viewpoint of restoring forces. In this paper, the case of $0 < \alpha < \pi$ is mainly discussed, but a similar discussion can be easily made for the other case of $\pi < \alpha < 2\pi$.

A new x axis pointing to the \mathbf{k} direction is taken,

which corresponds to the procedure to rotate the $x'y'z$ coordinates by the angle $-\beta$ around the y' axis (see Fig. 1). These new coordinates in which \mathbf{k} is expressed as $(\kappa (> 0), 0, 0)$ are hereafter referred to as $x''y'z''$ coordinates (Fig. 3). The linearized Boussinesq model equations are expressed in the following.

$$-F_z \tilde{v} + F_{y'} \tilde{w} - b \sin \beta + \frac{1}{\rho_0} \frac{\partial p}{\partial x''} = 0, \quad (2.6a)$$

$$\frac{\partial \tilde{v}}{\partial t} - F_{x'} \tilde{w} = 0, \quad (2.6b)$$

$$\frac{\partial \tilde{w}}{\partial t} + F_{x'} \tilde{v} - b \cos \beta = 0, \quad (2.6c)$$

$$\frac{\partial \tilde{u}}{\partial x''} = 0, \quad (2.6d)$$

$$\frac{\partial b}{\partial t} + N_0^2 \cos \beta \tilde{w} = 0, \quad (2.6e)$$

where $(\tilde{u}, \tilde{v}, \tilde{w})$ are the velocity components for (x'', y', z'') , and the i th (1–3) components of $2\mathbf{\Omega}$:

$$F_{x'} = 2\mathbf{\Omega} \cdot \mathbf{e}_{x'} = f_v \sin \beta + f_H \sin \alpha \cos \beta, \quad (2.7a)$$

$$F_{y'} = 2\mathbf{\Omega} \cdot \mathbf{e}_{y'} = f_H \cos \alpha, \quad (2.7b)$$

$$F_{z'} = 2\mathbf{\Omega} \cdot \mathbf{e}_{z'} = f_v \cos \beta - f_H \sin \alpha \sin \beta, \quad (2.7c)$$

where \mathbf{e}_i is the basis vector of the i th direction. The continuity equation (2.6d) indicates $\tilde{u} = 0$, which means that the parcel motion is only in the $y'z''$ plane (an equiphase surface) (Fig. 3). In other words, the inertia-gravity waves for $f_H \neq 0$ are transverse waves as in the case of $f_H = 0$. The x'' momentum equation (2.6a) determines the distribution of p so as to keep the tilt of the parcel motions. The restoring forces for parcels are the Coriolis force including the f_H -terms and the buoyancy force. The equation for \tilde{w} and the dispersion relation in the $x''y'z''$ coordinates become

$$\frac{\partial^2 \tilde{w}}{\partial t^2} = -(F_{x'}^2 + N_0^2 \cos^2 \beta) \tilde{w}, \quad (2.8)$$

$$\omega^2 = F_{x'}^2 + N_0^2 \cos^2 \beta. \quad (2.9)$$

Note that (2.9) is identical to (2.5). The equations (2.6b) and (2.8) imply that parcels rotate clockwise with time in the $y'z''$ plane, as seen from the $\mathbf{\Omega}_k$ direction (Fig. 3), where $\mathbf{\Omega}_k$ is the projection of $\mathbf{\Omega}$ onto the \mathbf{k} direction.

First, the case of $\hat{\omega} = \hat{\omega}_{\max}$ is considered. For $f_H = 0$, $\hat{\omega}_{\max}$ is N_0 , independent of α and latitude. For $f_H \neq 0$, this is not the case. When $0 \leq \beta < \pi/2$, $F_{x'} > f_v \sin \beta \geq 0$ because of non zero f_H (i.e., the tilt of $\mathbf{\Omega}$), as is evident from (2.7a) and Fig. 4a. This means that the f_H -effect facilitates the parcel motions. Thus, $\hat{\omega}$ takes its maximum, which is higher than N_0 . Since the Coriolis force is not perpendicular to the buoyancy force, unlike the case for $f_H = 0$ (see Figs. 5a, b), $\hat{\omega}_{\max}$ depends on N_0 ,

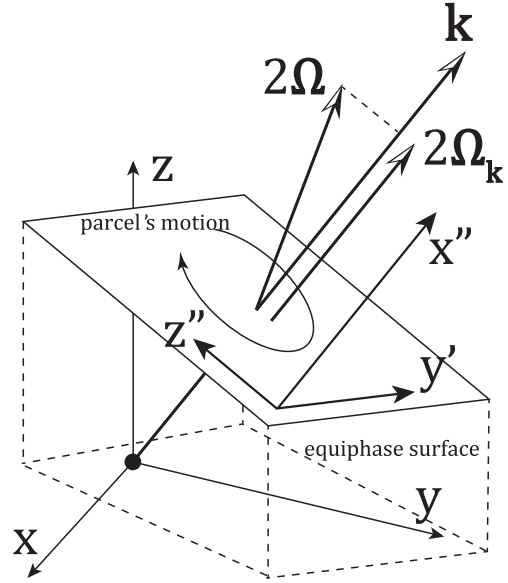


Fig. 3. Positional relation among wavevector \mathbf{k} , twice angular velocity of the Earth's rotation $\mathbf{\Omega}$, an equiphase surface, and xyz and $x''y'z''$ coordinates for $0 < \alpha < \pi/2$ and $0 < \beta < \pi/2$. The origins of xyz and $x''y'z''$ are taken to be the same, while that of $x''y'z''$ is shifted. The x'' axis points to the \mathbf{k} direction. The parcel rotates clockwise on the equiphase surface, seen from the $\mathbf{\Omega}_k$ direction, where $2\mathbf{\Omega}_k$ is the projection of $2\mathbf{\Omega}$ onto the \mathbf{k} direction.

α , and latitude. Note that both buoyancy and f_H -effects increase $\hat{\omega}$. For convenience of discussion below, we define β_{\max} as $\hat{\omega}(\beta_{\max}) = \hat{\omega}_{\max}$ for a given α . Note that m_{\max} in Fig. 2 is identical to $\kappa \sin \beta_{\max}$.

Second, the case of $\hat{\omega} = \hat{\omega}_{\min}$ is considered. For $f_H = 0$, $\hat{\omega}_{\min}$ is f_v , independent of α and N_0 . For $f_H \neq 0$, this is also not the case. When $-\pi/2 < \beta < \beta_{th}$, $|F_{x'}| < |f_v \sin \beta|$ because of non zero f_H (i.e., the tilt of $\mathbf{\Omega}$), as is evident from (2.7a) and Fig. 4b, where

$$\tan \beta_{th} = -\frac{f_H \sin \alpha}{2f_v}, \quad (2.10)$$

for $-\pi/2 < \beta_{th} < 0$. As \mathbf{k} becomes vertical ($\beta \rightarrow \pm \pi/2$), $\hat{\omega}$ approaches f_v because the buoyancy and f_H -effects become weaker. Since the Coriolis force is not perpendicular to the buoyancy force, unlike the case for $f_H = 0$ (Figs. 5a, c), $\hat{\omega}_{\min}$ depends on both N_0 and f_H . The f_H -effect decreases $\hat{\omega}$, while the buoyancy effect increases it. Thus, the magnitudes of the two effects have to be compared. The buoyancy effect, which is proportional to $\cos^2 \beta$ as in (2.9), becomes weak more rapidly than the f_H effect as $\beta \rightarrow -\pi/2$. Thus, $\hat{\omega}$ takes its minimum, which is lower than f_v , dependent of N_0 ,

$$\hat{\omega}_{\max, \min}^2 = \frac{N_0^2 + f_v^2 + f_{H\alpha}^2 \pm \sqrt{(N_0^2 - f_v^2 + f_{H\alpha}^2)^2 + 4f_{H\alpha}^2 f_v^2}}{2}, \quad (2.11)$$

$$f_{H\alpha} \equiv f_H \sin \alpha, \quad (2.12)$$

and those for β_{\max} and β_{\min} are calculated as

$$\begin{cases} \beta_{\max} = \gamma \\ \beta_{\min} = -\pi/2 + \gamma, \end{cases} \quad (2.13)$$

respectively, where

$$\gamma = \tan^{-1} \left(\frac{2f_{H\alpha} f_v}{(N_0 + f_{H\alpha} - f_v)^2 + \sqrt{(N_0^2 + f_{H\alpha}^2 - f_v^2)^2 + 4f_{H\alpha}^2 f_v^2}} \right). \quad (2.14)$$

Note that $\tan \gamma = m_{\max}/\tilde{k}$ and $-1/\tan \gamma = m_{\min}/\tilde{k}$. The formula (2.11) is equivalent to the expression obtained by Gerkema and Shrira (2005a) and Gerkema and Exarchou (2008). The meaning of (2.13) is that the wavenumber vector for $\hat{\omega}_{\max}$ is perpendicular to that for $\hat{\omega}_{\min}$.

Figure 6 shows the range of the internal wave frequency as a function of N_0 by shading for $\phi = 45^\circ$ and $\alpha = \pi/2$ as an example. It is important that $\hat{\omega}_{\min}$ monotonically increases with N_0 for $f_H \neq 0$, whereas it is constant ($= f_v$) for $f_H = 0$. In contrast, $\hat{\omega}_{\max}$ is a monotonically increasing function of N_0 whether $f_H = 0$ or not. This is because the f_H -effect weakens as N_0 increases, because stability suppresses the vertical motion. From Fig. 6 it is seen that waves whose frequencies are in the range of $f_v \leq \hat{\omega} \leq \hat{\omega}_{\max}|_{N_0=f_v}$ can oscillate in any stratification (Gerkema and Exarchou 2008). Another important implication of Fig. 6 is the existence of a wave solution trapped in the WSL, which has $\hat{\omega}$ higher than $\hat{\omega}_{\min}$ in the WSL and lower than $\hat{\omega}_{\min}$ outside the WSL.

2.3 Modification of the hodograph by the f_H -effect

The hodograph is frequently analyzed to examine the characteristics of the inertia-gravity waves. Gerkema and Exarchou (2008) showed that the major axis of the hodograph is not always parallel to \mathbf{k}_H for $f_H \neq 0$. However, they only argued about the shape of the hodograph using characteristic coordinates and did not discuss the rotational direction, which gives important information on wave propagation (e.g., Sato 1994). In this paper, modification of the rotational direction of the hodograph with time, as well as its shape, is examined as a function of $\hat{\omega}$ and m by using the $x'y'z$ coordinates, where the x' direction is the same as \mathbf{k}_H one.

The polarization of horizontal velocity for $f_H \neq 0$ is

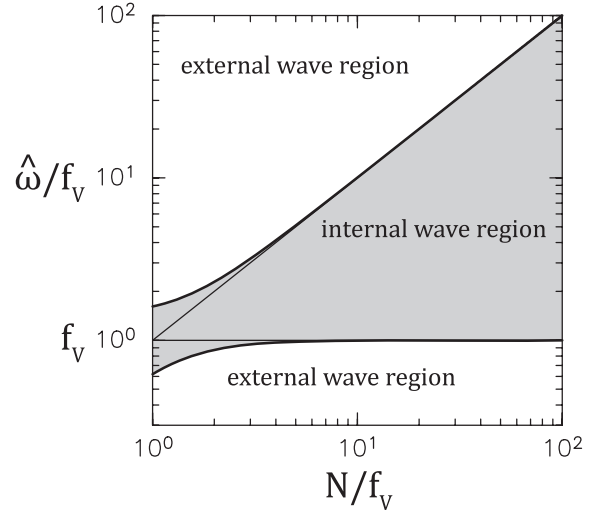


Fig. 6. Internal wave frequency ($\hat{\omega}/f_v$) range as a function of the buoyancy frequency (N_0/f_v) normalized by f_v for $\phi = 45^\circ$ and $\alpha = \pi/2$ for the $f_H \neq 0$ (shaded region).

$$\begin{aligned} \tilde{\mathbf{v}} &= -i \frac{f_v}{\hat{\omega}} \left[\frac{f_H \sin \alpha}{f_v} \frac{\tilde{k}}{m} + 1 \right] \tilde{\mathbf{u}} \\ &= -i \frac{f_v}{\hat{\omega}(\alpha, \beta)} \left[\frac{\sin \alpha}{\tan \phi \tan \beta} + 1 \right] \tilde{\mathbf{u}}. \end{aligned} \quad (2.15)$$

Here $\hat{\omega}$ is a function of α and β (see (2.3) and (2.5)). For $f_H \neq 0$, (2.15) is valid when $m \neq 0$ (i.e., $\beta \neq 0$). When $m = 0$, $\tilde{\mathbf{u}} = 0$, and $\tilde{\mathbf{v}} \neq 0$ ((2.2b) and (2.2d)) for $f_H \neq 0$, the polarization is linear, while there is no inertia-gravity wave solution at this limit for $f_H = 0$, but the hodograph approaches linear when $m \rightarrow 0$.

The shape and rotation of the hodograph with time are modified for $f_H \neq 0$, as illustrated in Fig. 2c, as a function of m . The hodograph is also linear when $\mathbf{k} \perp \boldsymbol{\Omega}$, because the Coriolis force does not act on parcels (Fig. 5d). The direction of the linear hodograph is parallel to \mathbf{k}_H . The vertical wave number (m_\perp) for $\mathbf{k} \perp \boldsymbol{\Omega}$ is expressed as

$$m_\perp = \kappa \sin \left[\tan^{-1} \left(\frac{-\sin \alpha}{\tan \phi} \right) \right]. \quad (2.16)$$

An important characteristic is that the rotational direction of the hodograph with time depends on ϕ and \mathbf{k} for $f_H \neq 0$. The rotation for $f_H = 0$ in NH is always clockwise because $\boldsymbol{\Omega}_k$ points to the negative \mathbf{k} direction for $m < 0$. The rotational direction of the hodograph with time for $f_H \neq 0$ is anticlockwise in a range of $m_\perp < m < 0$ and clockwise in the other ranges. This anticlockwise rotation for $m_\perp < m < 0$ corresponds to

the situation in which $\mathbf{\Omega}_k$ points to the \mathbf{k} direction due to the f_H -effect (i.e., the tilt of $\mathbf{\Omega}$) even when m is negative.

For $f_H = 0$, the long axis of the hodograph is always parallel to the \tilde{u} axis, i.e., \mathbf{k}_H . However, this is not the case for $f_H \neq 0$ (Gerkema and Exarchou 2008). The long axis of the hodograph is parallel to the \tilde{v} axis (i.e., perpendicular to \mathbf{k}_H) for $\hat{\omega} > N_0$, while it is parallel to the \tilde{u} axis (i.e., parallel to \mathbf{k}_H) for $\hat{\omega} < N_0$. When $\tilde{k} = 0$ (i.e., \mathbf{k} is vertical), $\hat{\omega} = f_v$ and the hodograph is a circle similarly to the case for $f_H = 0$. When $\hat{\omega} = N_0$, the hodograph is also a circle (Gerkema and Exarchou 2008), whose rotational direction is clockwise (anticlockwise) when $m > 0$ ($m < 0$). As the rotational direction changes at $m = m_\perp$ in which the hodograph is linear, m_\perp does not exceed m at which $\hat{\omega} = N_0$. Note that m_\perp approaches zero with $f_H \sin \alpha$.

2.4 Dependence of c_{gz} on c_{pz} modified by the f_H -effect

From Fig. 2a it is seen that when $f_H = 0$, the inertia-gravity waves exhibit the property that the sign of the vertical group velocity c_{gz} is always opposite to that of vertical phase speed c_{pz} . However, this is not the case for $f_H \neq 0$. Although the reason is mathematically clear ($0 < \beta_{\max} < \pi/2$, $-\pi/2 < \beta_{\min} < 0$ and $\hat{\omega} \rightarrow f_v$ as $\beta \rightarrow \pm \pi/2$), the physical mechanism is not clearly explained so far. Thus, an intuitive illustration is given in this study in terms of the form stress over the potential temperature surface (Θ surface).

a. Consideration in terms of energy flux

The vertical energy flux in the Boussinesq model is related to c_{gz} as²

$$\overline{p\bar{w}} = E c_{gz}, \quad (2.17)$$

where an the overbar denotes a horizontal average over the wavelength (e.g., Vallis 2006), and E is

$$E = \frac{\rho_0}{2} [u^2 + v^2 + w^2 + (b/N)^2]. \quad (2.18)$$

Thus, $\text{sgn}(c_{gz})$ is equal to that of $\overline{p\bar{w}}$. Note that (2.17) holds also for equatorial waves after integrating with respect to latitude (Andrews et al. 1987). An examination is made on the $x'y'z$ coordinates, in which the form stress has the x' component only. Using $w \equiv D\zeta/Dt = \partial\zeta/\partial t$, where ζ is vertical displacement of the

parcels, the vertical energy flux is written as

$$E c_{gz} = \overline{p\bar{w}} = \left(\frac{\hat{\omega}}{\tilde{k}} \right) \left(-p \overline{\frac{\partial\zeta}{\partial x'}} \right) = \hat{c} \left(-p \overline{\frac{\partial\zeta}{\partial x'}} \right), \quad (2.19)$$

where $\hat{c} (> 0)$ is the horizontal phase speed. The right-hand side of (2.19) expresses the rate of work done by the form stress over the wavy Θ surface moving toward the x' direction with a speed of \hat{c} .

1) Case of $f_H = 0$

As space is horizontally isotropic for $f_H = 0$, the form stress does not depend on the horizontal direction (α in Fig. 1). The relation between p and ζ is obtained by (2.2c) and (2.2e) when $m \neq 0$:

$$p = \frac{\rho_0}{\tilde{k}m} (N_0^2 - \hat{\omega}^2) \frac{\partial\zeta}{\partial x'}. \quad (2.20)$$

Thus, the vertical energy flux becomes

$$\overline{p\bar{w}} = -\hat{c} \cdot \frac{\rho_0(N_0^2 - \hat{\omega}^2)}{\tilde{k}m} \left(\overline{\frac{\partial\zeta}{\partial x'}} \right)^2 = -c_{pz} \cdot \frac{\rho_0(N_0^2 - \hat{\omega}^2)}{\tilde{k}^2} \left(\overline{\frac{\partial\zeta}{\partial x'}} \right)^2. \quad (2.21)$$

Because $\hat{\omega} < N_0$, (2.21) indicates that $\text{sgn}(\overline{p\bar{w}})$, and hence $\text{sgn}(c_{gz})$, is opposite to $\text{sgn}(c_{pz})$. If the hydrostatic balance can be assumed, $\hat{\omega}$ in (2.20) and (2.21) can be neglected.

More importantly, it should be noted here that this relation generally holds for all plane waves in linearized Boussinesq and primitive equation (using the log p height) systems on beta planes, because (2.21) is derived only from the vertical momentum and thermodynamic equations. Moreover, this relation holds also for the equatorial waves, because a meridional structure is not assumed to derive (2.21), and (2.21) can be integrated with respect to the meridional direction. Note that the relation $\text{sgn}(c_{gz}) = -\text{sgn}(c_{pz})$ has been derived using the dispersion relation of each wave so far.

When $m = 0$, the relation between p and ζ is derived from the horizontal momentum equations, depending on the models. However, considering the continuity of the dependence of the vertical energy flux on m , it is clear that $c_{gz} = 0$ when $m = 0$ for the Boussinesq fluid.

2) Case of $f_H \neq 0$

As space is not horizontally isotropic for $f_H \neq 0$, the form stress depends on the \mathbf{k}_H direction (i.e., α). The energy flux is separately examined for $m \neq 0$ and $m = 0$. For $m \neq 0$, using (2.2c), (2.2d), and (2.2e),

²Even when $f_H = 0$, the horizontal energy flux (pu , $p\nu$) of Rossby waves is not proportional to the horizontal group velocity because of the ageostrophic velocity components, whose magnitudes are proportional to y on the beta plane (Pedlosky 1987).

$$\overline{p\omega} = -\hat{c} \frac{\rho_0}{\tilde{k}m} \left[(N_0^2 - \hat{\omega}^2) \left(\frac{\partial \xi}{\partial x'} \right)^2 + f_H \sin \alpha \frac{\partial \tilde{v}}{\partial x'} \frac{\partial \xi}{\partial x'} \right]. \quad (2.22)$$

Using (2.2b) and (2.2d),

$$\tilde{v} = \left(f_H \sin \alpha + \frac{f_H m}{\tilde{k}} \right) \xi. \quad (2.23)$$

Thus, (2.22) is written as

$$\overline{p\omega} = -\hat{c} \frac{\rho_0}{\tilde{k}m} \left[N_0^2 - \hat{\omega}^2 + f_H \sin \alpha \left(f_H \sin \alpha + \frac{f_H m}{\tilde{k}} \right) \right] \left(\frac{\partial \xi}{\partial x'} \right)^2. \quad (2.24)$$

For $0 < \alpha < \pi$ (i.e., $\sin \alpha > 0$), (2.24) indicates that $\text{sgn}(\overline{p\omega})$, i.e., $\text{sgn}(c_{gz})$, is the same as $\text{sgn}(c_{pz})$ when $m < m_{th}(\hat{\omega}, \tilde{k}, \alpha)$, where

$$m_{th}(\hat{\omega}, \tilde{k}, \alpha) = -\tilde{k} \frac{N_0^2 - \hat{\omega}^2 + (f_H \sin \alpha)^2}{f_H f_H \sin \alpha}. \quad (2.25)$$

Using (2.9), it is shown that β s which satisfy $m = m_{th}(\hat{\omega}(\alpha, \beta), \tilde{k}, \alpha)$ are β_{\max} and β_{\min} . The condition $m < m_{th}(\hat{\omega}(\alpha, \beta), \tilde{k}, \alpha)$ is equivalent to $m < m_{\min} < 0$ or $0 < m < m_{\max}$. Thus, the reason for the changes of $\text{sgn}(c_{gz})$ at $\hat{\omega}_{\min}$ and $\hat{\omega}_{\max}$ is that the f_H -effect reverses the direction of the form stress at these frequencies. For $\pi < \alpha < 2\pi$ (i.e., $\sin \alpha < 0$), the same results are obtained except that the condition $m < m_{th}(\hat{\omega}(\alpha, \beta), \tilde{k}, \alpha)$ is replaced with $m > m_{th}(\hat{\omega}(\alpha, \beta), \tilde{k}, \alpha)$.

Next, for $m = 0$, the relation between p and ξ is obtained by using the x' momentum equation instead of the vertical one. In this case, $\tilde{u} = 0$ from (2.2d). From (2.2a), we obtain

$$\frac{\partial p}{\partial x'} = \rho_0 f_H \tilde{v} - \rho_0 f_H \cos \alpha \frac{\partial \xi}{\partial t}. \quad (2.26)$$

The vertical energy flux is expressed as

$$\overline{p\omega} = \hat{c} \left(\rho_0 f_H \tilde{v} \xi \right). \quad (2.27)$$

Using (2.23), the vertical energy flux is written as

$$\overline{p\omega} = \hat{c} \left(\rho_0 f_H f_H \sin \alpha \xi^2 \right). \quad (2.28)$$

The equation (2.28) indicates that c_{gz} is positive (negative) when $\sin \alpha > (<) 0$ (Fig. 2a).

b. Intuitive illustration

In this subsection, the relation between $\text{sgn}(c_{gz})$ and $\text{sgn}(c_{pz})$ is examined in terms of the vertical force balance (2.2c). First, the case of $f_H = 0$ is considered. In this case, $\hat{\omega} < N_0$, which means that the magnitude of the buoyancy force is always greater than that of $-\partial w / \partial t$. Thus, the vertical pressure gradient force is

always opposite to the buoyancy force to keep the balance (Fig. 7a). For $m < 0$ (i.e., $c_{pz} < 0$), constant phase lines tilt against the x' direction with height. Because of the direction of the vertical pressure gradient force, p is distributed as illustrated in Fig. 7a. As the regions of negative p and positive $\partial \xi / \partial x'$ accord, the form stress points to the x' direction. The Θ surface does positive work on the fluid above, and hence, c_{gz} is positive. Similarly it is understood that c_{gz} is negative for $c_{pz} > 0$.

Second, the case of $f_H \neq 0$ and $m \neq 0$ is considered. For simplicity, we set $\alpha = \pi/2$ (i.e., \mathbf{k}_H points northward) because the f_H -effect is the largest in this case, namely $f_H \cos \alpha \tilde{u} = 0$ and $f_H \sin \alpha \tilde{v} = f_H \tilde{v}$ in (2.2c). The cases of $m < m_{\min}$ and $0 < m < m_{\max}$ are mainly considered because the cases of $m_{\min} < m < 0$ and $m_{\max} < m$ are similar to the cases of $m < 0$ and $m > 0$ for $f_H = 0$, respectively. For $m < m_{\min}$ in which the parcel trajectories are nearly horizontal, the balance between the Coriolis force and the vertical pressure gradient force is dominant. Note that the parcel moves clockwise, seen from the $\mathbf{\Omega}_k$ direction as in Fig. 7b, illustrating the distribution of \tilde{v} on the Θ surface. The Θ surface does negative work on the fluid above, indicating that c_{gz} is negative.

For $0 < m < m_{\max}$ in which the parcel trajectories are nearly vertical, the magnitude of $-\partial w / \partial t$ is greater than that of the sum of the buoyancy and Coriolis forces due to the f_H -effect. Thus, the vertical pressure gradient force must be opposite to $-\partial w / \partial t$ (Fig. 7c). The Θ surface does positive work on the fluid above, indicating that c_{gz} is positive.

Third, the case of $f_H \neq 0$ and $m = 0$ is considered (Fig. 7d). Because there is no vertical pressure gradient, the horizontal force balance determines c_{gz} and the distribution of p . In this case, $\tilde{u} = 0$ in (2.2d), and hence, \tilde{v} is induced by the f_H -effect ((2.2b) and (2.2c)). The Coriolis force $f_H \tilde{v}$ is opposite to the horizontal pressure gradient $-\frac{1}{\rho_0} \frac{\partial p}{\partial x'}$ in (2.2a). The Θ surface does positive work on the fluid above. Thus, c_{gz} is positive. Note that \tilde{v} is always zero for $f_H = 0$, and hence, p is also zero. Thus, the Θ surface does no work on the fluid above, and hence, c_{gz} is always zero.

When $\alpha = -\pi/2$, the directions of the form stress are opposite to those in Figs. 7b–7d. Thus, $\text{sgn}(c_{gz})$ is also opposite in all cases. When $\alpha \neq \pm \pi/2$, $f_H \cos \alpha \tilde{u}$ in (2.2c) and $f_H \cos \alpha w$ in (2.2a) are not zero. However, \tilde{u} and w are zero at the top and bottom of the wavy Θ surface (that is, the minimum and maximum phases of ξ). Thus, the same explanation as for $\alpha = \pm \pi/2$ can be given.

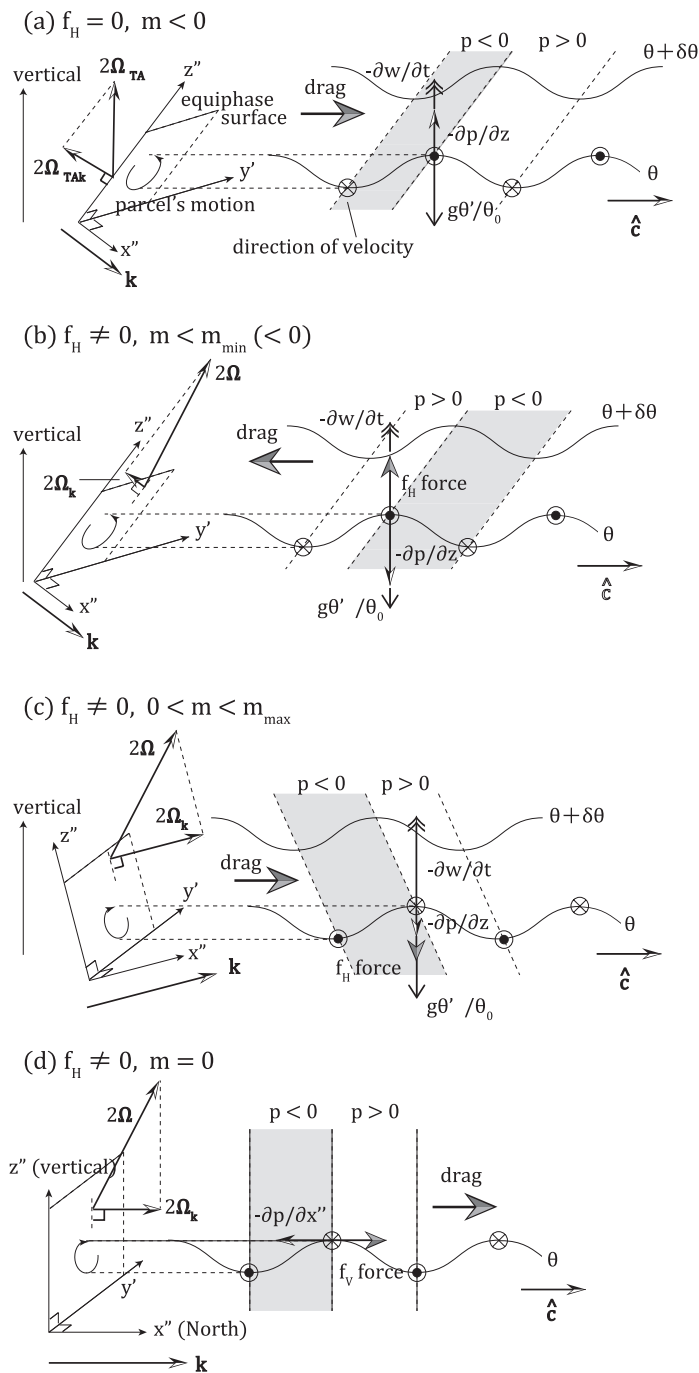


Fig. 7. Force balance on the Θ surface (a) when $f_H = 0, m < 0$, (b) when $f_H \neq 0, m < m_{\min} < 0$, (c) when $f_H \neq 0, 0 < m < m_{\max}$, and (d) when $f_H \neq 0, m = 0$. Right figures show y' cross sections of the Θ surfaces and the force balances, and left figures show the parcel motions projected onto the $y'z''$ planes (equiphase surfaces). The arrow labeled \hat{c} for each figure shows the velocity of the Θ surface. Note that scales of arrows showing the buoyancy force are different for respective figures.

3. Presence of trapped inertia-gravity waves in the WSL

3.1 Necessary conditions for the existence of trapped solutions

According to Durran and Bretherton (2004), the necessary condition for the existence of sub-inertial modes in the vertically bounded domain is that the frequency takes its minimum at a finite vertical wave number in the dispersion curve. The sub-inertial modes consist of two plane waves whose $\hat{\omega}$ ($> \hat{\omega}_{\min}$) are the same but the signs of c_{gz} are opposite, although magnitudes of the two c_{gz} may be different. However, this condition is not sufficient for the existence of trapped waves in the WSL in the fluid. The condition that the minimum frequency is a monotonically increasing function of N_0 is also necessary, because the amplitude of wave must decrease outside the WSL, as shown in Subsection 2.2.

3.2 Trapped solution in the idealized WSL

An analytic solution trapped in the WSL is examined for an idealized distribution of N having a form of a square well with a width of $2a$, as shown in Fig. 8. Considering the solutions with the shape of

$$(u, v, w, b, p/\rho_0) = [U(z), iV(z), iW(z), b(z), P(z)] \exp i(kx + ly - \hat{\omega}t), \quad (3.1)$$

in the xyz coordinates, a single equation for W is obtained (Kasahara 2003; Gerkema and Shrira 2005a):

$$\frac{d^2 W}{dz^2} + 2 \frac{if_v f_H}{f_v^2 - \hat{\omega}^2} \frac{dW}{dz} + \frac{(\hat{\omega}^2 - N(z)^2)(k^2 + l^2) - l^2 f_H^2}{f_v^2 - \hat{\omega}^2} W = 0, \quad (3.2)$$

where $\hat{\omega} \neq f_v$ is assumed. Note that the original Cartesian coordinates (xyz) are used. Following Kasahara (2003), $W(z)$ is written as follows.

$$W(z) = \psi(z) \exp i\Gamma z, \quad (3.3)$$

$$\Gamma \equiv -\frac{lf_v f_H}{f_v^2 - \hat{\omega}^2}, \quad (3.4)$$

where $\psi(z)$ is the envelope function of W . Defining E and $V(z)$ as

$$E \equiv \Gamma^2 + \frac{\hat{\omega}^2(k^2 + l^2) - l^2 f_H^2}{f_v^2 - \hat{\omega}^2}, \quad (3.5a)$$

$$V(z) \equiv N(z)^2 \frac{k^2 + l^2}{f_v^2 - \hat{\omega}^2}, \quad (3.5b)$$

respectively, the equation of $\psi(z)$ is obtained from

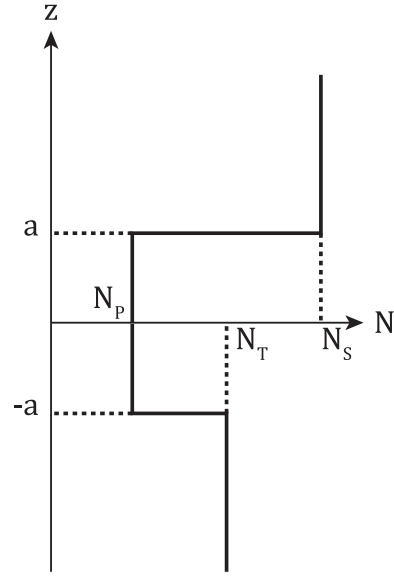


Fig. 8. Vertical profile of N having the form of a square well.

(3.2):

$$-\frac{d^2}{dz^2} \psi + V(z) \psi = E \psi, \quad (3.6)$$

which is similar to Schrödinger's equation in a square well potential $V(z)$. Note that E does not explicitly depend on $N(z)$ but implicitly does through $\hat{\omega}$. For the trapped solution, $\hat{\omega}$ is decided by the boundary conditions at $z = \pm a$. The equation (3.6) indicates that ψ oscillates where $E > V(z)$ and decays exponentially where $E < V(z)$.

Wave solutions trapped in the WSL are present when $V(N_T) > E$, $V(N_S) > E$, and $V(N_P) < E$. The solutions in the respective ranges are

$$\psi(z) = \begin{cases} A \exp\left(\frac{z}{H_T}\right) & (z < -a), \\ B \exp(i\mu z) + C \exp(-i\mu z) & (-a \leq z \leq a), \\ D \exp\left(-\frac{z}{H_S}\right) & (a < z), \end{cases} \quad (3.7)$$

where A , B , C , and D are constant complex numbers, and H_T , H_S , and μ are, respectively, defined as

$$H_T \equiv [V(N_T) - E]^{-1/2}, \quad (3.8a)$$

$$H_S \equiv [V(N_S) - E]^{-1/2}, \quad (3.8b)$$

$$\mu \equiv [E - V(N_P)]^{1/2}. \quad (3.8c)$$

By using boundary conditions that pressure and vertical velocity, i.e., ψ and $d\psi/dz$, are continuous at $z = \pm a$ and evanescent for $|z| \rightarrow \infty$, we obtain

Table 1. Values of $\hat{\omega}/f_v$, $2\pi/\mu$, $2\pi/\Gamma$, H_s , H_T , and c_{gz} for (a) $\lambda_y = 500$ km, (b) $\lambda_y = 1000$ km, and (c) $\lambda_y = 3000$ km for the trapped wave solution of SI = 1–4, assuming that $a = 1.5$ km, $k = 0$, $\phi = 45^\circ$, $N_s = 200 f_v$, $N_T = 100 f_v$, and $N_p = 50 f_v$. c_{gz} is vertical group velocity of plane waves that comprise the trapped waves.

(a) $\lambda_y = 500$ km						
SI	$\hat{\omega}/f_v$	$2\pi/\mu$ (km)	$2\pi/\Gamma$ (km)	H_s (km)	H_T (km)	c_{gz} (m/day)
1	0.9998002	6.053	−0.200	8.215E-03	1.837E-02	3.99E-03 / −3.49E-03
2	0.9998008	3.027	−0.199	8.202E-03	1.835E-02	8.46E-03 / −6.50E-03
3	0.9998019	2.018	−0.198	8.182E-03	1.832E-02	1.34E-02 / −9.03E-03
4	0.9998034	1.513	−0.197	8.154E-03	1.827E-02	1.88E-02 / −1.11E-02
(b) $\lambda_y = 1000$ km						
SI	$\hat{\omega}/f_v$	$2\pi/\mu$ (km)	$2\pi/\Gamma$ (km)	H_s (km)	H_T (km)	c_{gz} (m/day)
1	0.9998008	6.106	−0.398	1.640E-02	3.670E-02	1.68E-02 / −1.29E-02
2	0.9998033	3.053	−0.393	1.631E-02	3.655E-02	3.72E-02 / −2.21E-02
3	0.9998072	2.035	−0.386	1.616E-02	3.632E-02	6.07E-02 / −2.82E-02
4	0.9998121	1.526	−0.376	1.597E-02	3.601E-02	8.66E-02 / −3.17E-02
(c) $\lambda_y = 3000$ km						
SI	$\hat{\omega}/f_v$	$2\pi/\mu$ (km)	$2\pi/\Gamma$ (km)	H_s (km)	H_T (km)	c_{gz} (m/day)
1	0.9998073	6.314	−1.160	4.853E-02	1.090E-01	1.75E-01 / −8.31E-02
2	0.9998228	3.151	−1.063	4.662E-02	1.061E-01	4.10E-01 / −1.01E-01
3	0.9998413	2.096	−0.952	4.431E-02	1.028E-01	6.52E-01 / −9.18E-02
4	0.9998585	1.568	−0.849	4.205E-02	9.988E-02	8.73E-01 / −7.74E-02

$$\psi(z) = \begin{cases} D \left[\mu H_T \sin(2\mu a) - \frac{H_T}{H_s} \cos(2\mu a) \right] \exp \left[-a \left(\frac{1}{H_s} - \frac{1}{H_T} \right) \right] \exp \left(\frac{z}{H_T} \right) & (z < -a), \\ D \left[\cos \mu(z-a) - \frac{1}{\mu H_s} \sin \mu(z-a) \right] \exp \left(-\frac{a}{H_s} \right) & (-a \leq z \leq a), \\ D \exp \left(-\frac{z}{H_s} \right) & (a < z). \end{cases} \quad (3.9)$$

The equation for $\hat{\omega}$ is

$$\tan(2\mu a) = -\frac{H_T + H_s}{1/\mu - \mu H_s H_T}. \quad (3.10)$$

Note that H_s , H_T , and μ are functions of $\hat{\omega}$. Table 1 shows $\hat{\omega}$ and other related parameters for solution indexes (SI) of 1–4 and for a few meridional wavelengths λ_y ($\equiv 2\pi/l$) = 500, 1000, and 3000 km, where SI is defined as the number indicating the order of $\hat{\omega}$ for the solution and is approximately equal to the number of crests (or troughs) of ψ . Here we took $a = 1.5$ km, $k = 0$, $\phi = 45^\circ$, $N_s = 200 f_v$, $N_T = 100 f_v$, and $N_p = 50 f_v$ as an example. Note that the vertical

wavelength of w is $2\pi/\Gamma$, while that of ψ is $2\pi/\mu$. Figure 9 illustrates w in the y - z section and envelope ψ as a function of z for SI = 1–4.

Several important characteristics of the trapped wave solutions in the WSL are described below.

- Frequencies of the solutions satisfy $\hat{\omega} \lesssim f_v$.
- Values of $\hat{\omega}$ are discrete because of the boundary conditions on the edges of the WSL.
- As $\hat{\omega}$ increases, μ and SI increase.
- Inclination of phase lines with respect to the y axis is positive, independent of k and l :

$$-\frac{l}{\Gamma} = \frac{f_v^2 - \hat{\omega}^2}{f_v f_H} > 0. \quad (3.11)$$

- Solutions generally have fine vertical structures. The vertical wavelength ($2\pi/\Gamma$) decreases when the k_H direction approaches the x axis.

According to (3.7) and (3.9), the solution is composed of two plane waves having vertical wave numbers of $\Gamma - \mu$ and $\Gamma + \mu$ in the WSL, which have the same frequencies and are lower than f_v . These plane waves have finite c_{gz} even at $z = \pm a$ so that modes are formed in the WSL.

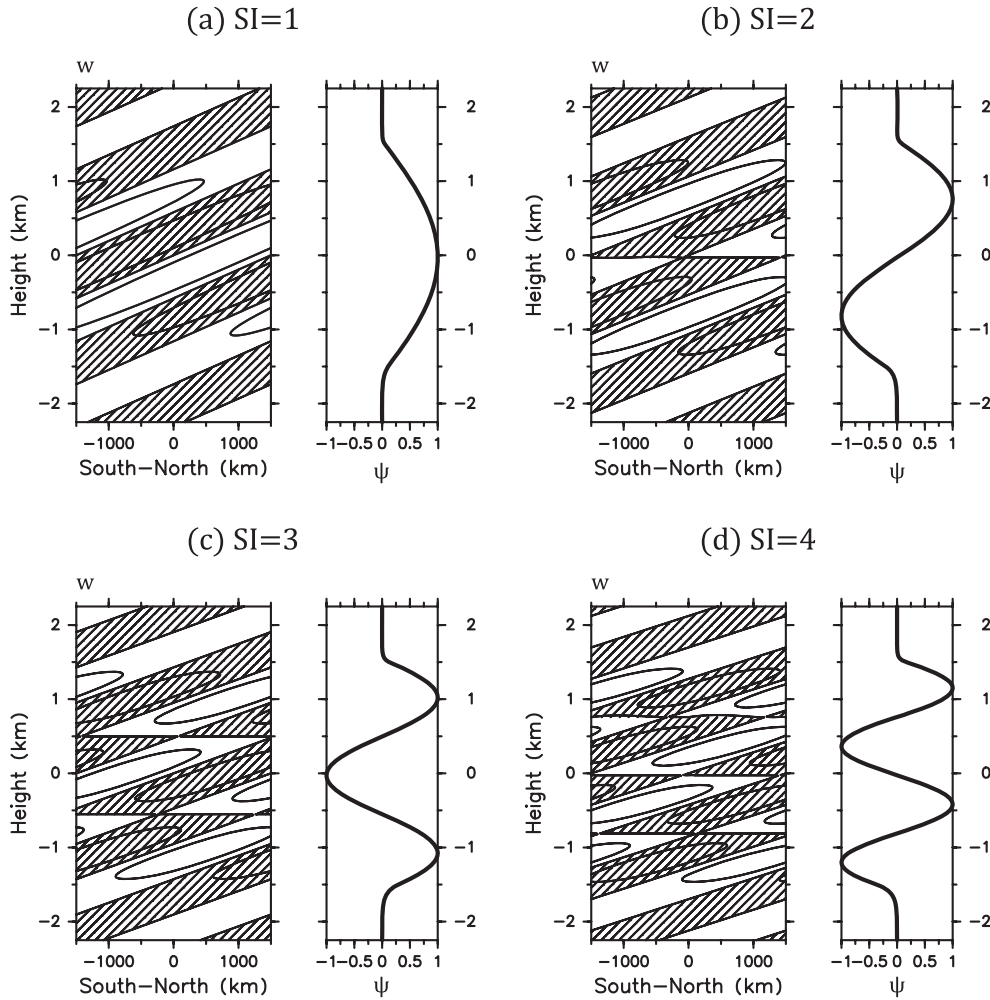


Fig. 9. Vertical wind component w in the y - z section (left) and envelope ψ as a function of z (right) for trapped wave solutions of $SI = 1$ –4, assuming that $a = 1.5$ km, $k = 0$, $l = 2\pi/3000$ km, $\phi = 45^\circ$, $N_s = 200 f_V$, $N_T = 100 f_V$, and $N_P = 50 f_V$. Contour intervals for w are half of the maximum of w for each case.

4. The f_H -effect on inertia-gravity waves in the real atmosphere

In this section, we discuss the degree of importance of the f_H -effect on the inertia-gravity waves in the real atmosphere. First, the structure of N in the meridional cross section is shown from the observation. Next, using the observed N structure around the tropopause, the f_H -effect on the hodograph and the possibility of the presence of the trapped inertia-gravity waves are examined. Note that the f_H -effect weakens as N increases.

4.1 Structure of N in the meridional cross section

Twice-daily radiosonde data obtained operationally

by the Japan Meteorological Agency (JMA) are used for the analysis of the N structure. The vertical intervals are approximately 200 m for temperature. The accuracy of temperature measurement is approximately 0.1 K (Japan Meteorological Agency 1995). The data were interpolated at a uniform vertical interval of 200 m using the cubic spline method to make further analysis easier.

Figure 10a shows the meridional cross section of N averaged for a summer period from June to August in 2007. Radiosonde data at stations distributed in the latitude range of 24.3°N – 43.3°N are used following the study by Sato and Dunkerton (2002). Crosses denote the tropopause heights at respective stations. Figures 10b and 10c show the mean vertical profiles of N for

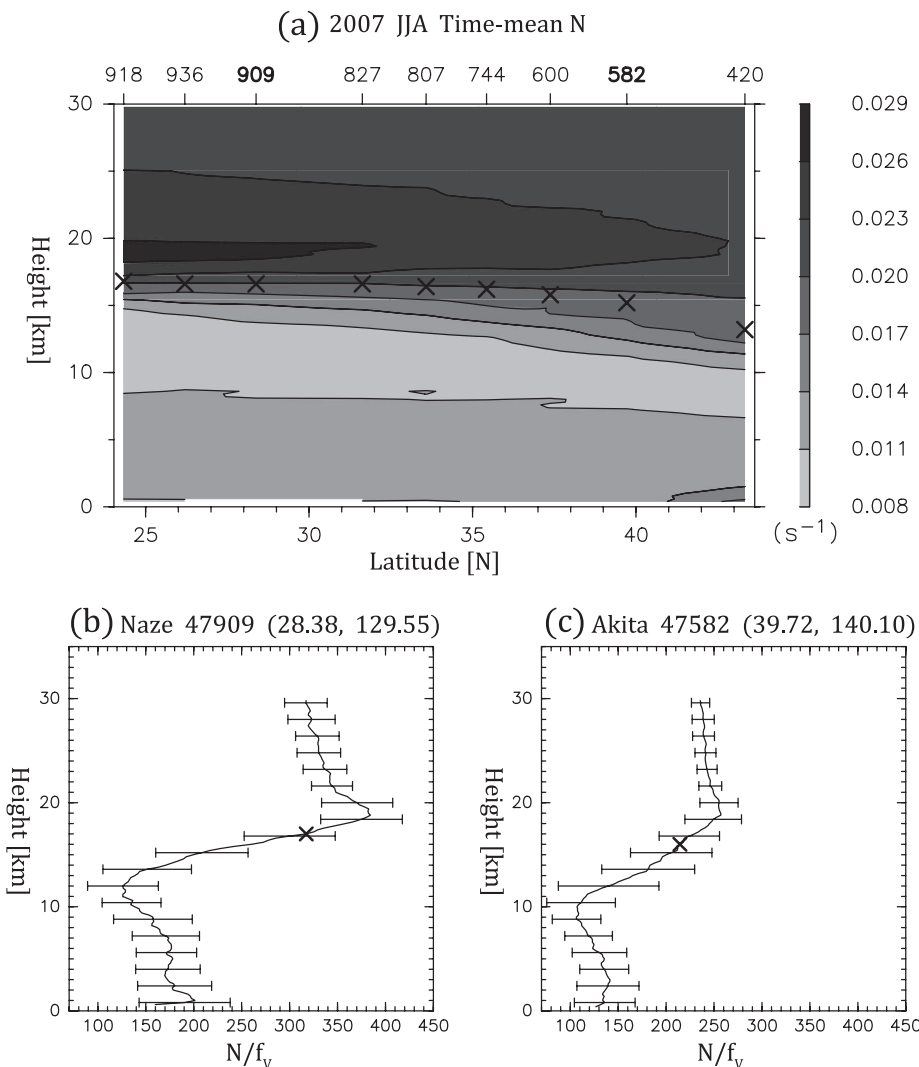


Fig. 10. (a) Latitude–height cross section of buoyancy frequency N averaged for June through August in 2007. (b) Vertical profiles averaged over the same period at Naze (28.4°N, 129.5°E, station number 47909) and (c) at Akita (39.7°N, 140.1°E, station number 47582), as typical examples for stations at low and high latitudes. Labels on the top axis in (a) denote the locations of respective stations (station number 47xxx). Contour intervals are 0.003 s^{-1} in (a). Crosses in all figures denote the tropopause heights at respective stations. Horizontal bars in (b) and (c) show the standard deviation of N/f_v .

the same period at low latitude (Naze; 28.4°N, 129.5°E) and high latitude (Akita; 39.7°N, 140.1°E) stations. Horizontal bars show the standard deviation. It is clear that there is a persistent WSL slightly below the tropopause. A similar WSL is observed for the summer periods of the other years (not shown). Figure 10a also indicates that the WSL is wider, and the minimum N values are smaller at lower latitudes. In the winter period from December to February, the WSL is narrower in the south region of Japan (24.3°N–30.0°N), and sometimes obscure in the north region (30.0°N–

43.3°N) (not shown).

As the tropopause height changes with time, the mean N structure shown in Fig. 10 may be smeared. Thus, we obtained the minimum of N^2 that exists in the height range of 8 km below the tropopause for each observation, which is referred to as $(N_{\min}^{\text{inst}})^2$. Figures 11a and 11b show the frequency distributions of $N_{\min}^{\text{inst}}/f_v$ at Naze and Akita, respectively. It is seen that the frequency $N_{\min}^{\text{inst}}/f_v$ is distributed around 80 ($N_{\min} \approx 0.005 s^{-1}$) at Naze and around 65 ($N_{\min} \approx 0.006 s^{-1}$) at Akita. Here N_{\min} is defined as the most frequent value of N_{\min}^{inst} .

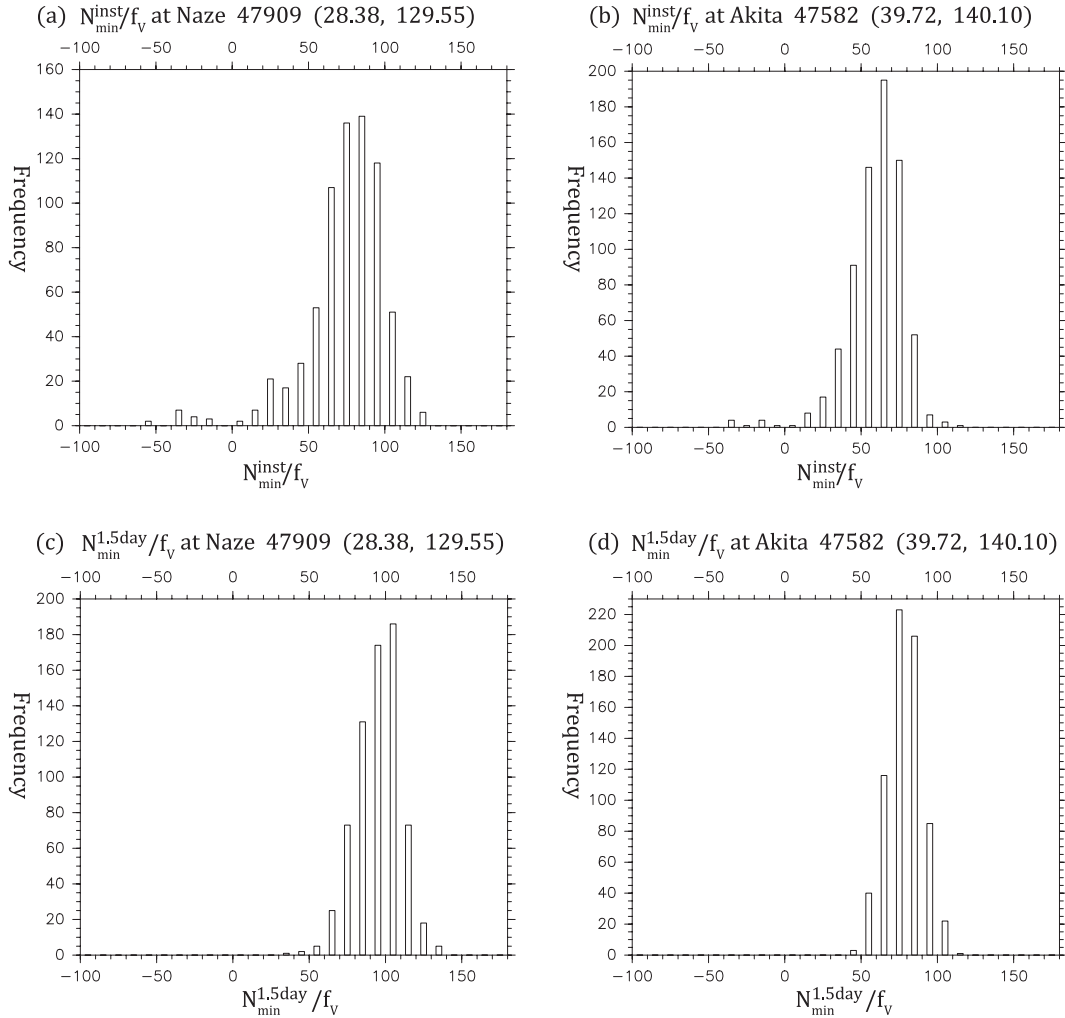


Fig. 11. (a) and (c) Frequency distributions of $N_{\min}^{\text{inst}}/f_v$ and $N_{\min}^{1.5\text{day}}/f_v$ for June through August in 2005–2008 at Naze (28.4°N, 129.5°E), respectively. (b) and (d) The same as (a) and (c) but for Akita (39.7°N, 140.1°E). See text for details. When $(N_{\min}^{\text{inst}}/f_v)^2$ is negative, $N_{\min}^{\text{inst}}/f_v$ is shown by $-\sqrt{|(N_{\min}^{\text{inst}}/f_v)^2|}$. Thus, the negative $N_{\min}^{\text{inst}}/f_v$ values mean convective instability.

Note that N_{\min} in the mid-latitudes is about a half times as low as a typical tropospheric value ($\sim 0.01 \text{ s}^{-1} \approx 100 f_v$). It is also seen that $(N_{\min}^{\text{inst}})^2$ is sometimes zero and even negative, indicating that convective instability occurs slightly below the tropopause. The instantaneous vertical profile of N may contain disturbances whose periods are approximately one day and less. To reduce their amplitudes, $(N_{\min}^{1.5\text{day}})^2$ is also defined as the minimum of the 1.5-day running mean vertical profile of N^2 in the height range of 8 km below the tropopause. Figures 11c and 11d show the frequency distributions of $N_{\min}^{1.5\text{day}}/f_v$ at Naze and Akita, respectively. It is seen that $N_{\min}^{1.5\text{day}}$ values are sometimes close to N_{\min} . Thus, N_{\min} ($\approx 50 f_v$) is used as the possible minimum value of

the background N in the WSL for the disturbances for further analysis.

4.2 The f_H -effect on the hodograph in the real atmosphere

As shown in Subsection 2.3 and 2.4, the characteristics of the hodograph for $f_H \neq 0$ are different from those of the hodograph for $f_H = 0$ where $\hat{\omega} > N_0$, $0 < m < m_{\max}$ ($m_{\max} < m < 0$), $m < m_{\min} < 0$ ($0 < m_{\min} < m$), or $m_{\perp} < m < 0$ ($0 < m < m_{\perp}$) for $0 < \alpha < \pi$ ($\pi < \alpha < 2\pi$). Figure 12 shows $\hat{\omega}$ as a function of m normalized by \bar{k} for $f_H \neq 0$, $N_0 = 50 f_v$, indicating that $\hat{\omega}_{\max} \approx N_0$ and $m_{\max} \approx 0$ in the real atmosphere. Thus, the area where $\hat{\omega} > N_0$ and $0 < m < m_{\max}$ is quite narrow. On the other

hand, m_{\min} and m_{\perp} may be important parameters to consider the f_H -effect in the real atmosphere. Figures 13a and 13b, respectively, show $\lambda_{\min} \equiv 2\pi/m_{\min}$ and $\lambda_{\perp} \equiv 2\pi/m_{\perp}$ as a function of $\lambda_H \equiv 2\pi/|k_H|$ and latitude for $\alpha = 90^\circ$ and $N_0 = 0.005 \text{ s}^{-1}$ (i.e., $N_0 \approx 50 f_V$ at $\phi = 45^\circ$). Note that λ_{\perp} does not depend on N_0 as in (2.16). Figure 13b indicates that λ_{\perp} is comparable to λ_H , which may be rare in the real atmosphere. On the other hand, there are possible cases in the real atmosphere, e.g., $\lambda_{\min} = O(100 \text{ m})$ for $\lambda_H = O(100 \text{ km})$. In such cases, we need to be careful for the treatment because they show different characteristics from those analyzed neglecting the f_H -effect where $\text{sgn}(c_{gz}) = \text{sgn}(c_{pz})$. Figures 11c and 11d show that $N_{\min}^{1.5\text{day}}$ can be less than $50 f_V$. Thus, it is necessary to examine the magnitude of N for the hodograph analysis.

4.3 Possibility of the presence of trapped inertia-gravity waves in the real atmosphere

It was shown that there is a persistent WSL slightly below the tropopause. Thus, the possibility of the presence of the inertia-gravity waves trapped there is examined in terms of the magnitude of c_{gz} . Table 1 shows the values of c_{gz} of the plane waves that comprise the trapped wave. As the magnitude of c_{gz} is smaller than 1 m day^{-1} in all cases, it takes quite a long time to form the trapped wave. If the trapped wave is formed within a few days, it is necessary that the characteristic magnitude of c_{gz} is greater than 100 m day^{-1} for the characteristic width of the WSL of 1 km . Using c_{gz} derived from (2.5), N_0 should be smaller than 0.001 s^{-1} ($\approx 10 f_V$):

$$c_{gz} = \frac{(f_H l + f_V m) [f_V (k^2 + m^2) - f_H l m] - N_0^2 m (k^2 + l^2)}{(k^2 + l^2 + m^2)^2 \hat{\omega}} \sim -\frac{f_V f_H l m^2 + N_0^2 m (k^2 + l^2)}{m^4 \hat{\omega}}, \quad (4.1)$$

for typical scales $k, l \sim 2\pi/100 \text{ km}$, $m \sim 2\pi/1 \text{ km}$, $\hat{\omega} \sim f_V$, and $f_H \sim f_V \sim 10^{-4} \text{ s}^{-1}$. Thus, it is concluded that in the WSL with $N_{\min} \approx 50 f_V$ slightly below the tropopause, such trapped waves are rarely observed.

5. Summary and concluding remarks

By using the linearized Boussinesq model containing f_H -terms, the characteristics of the inertia-gravity waves modified by the f_H -effect have been examined. The f_H -effects on the inertia-gravity waves are summarized as follows.

1. For $f_H = 0$, $f_V < \hat{\omega} < N_0$. However, for $f_H \neq 0$, the minimum frequency is lower than f_V , and the maximum is higher than N_0 . The vertical wave number is finite at the minimum frequency

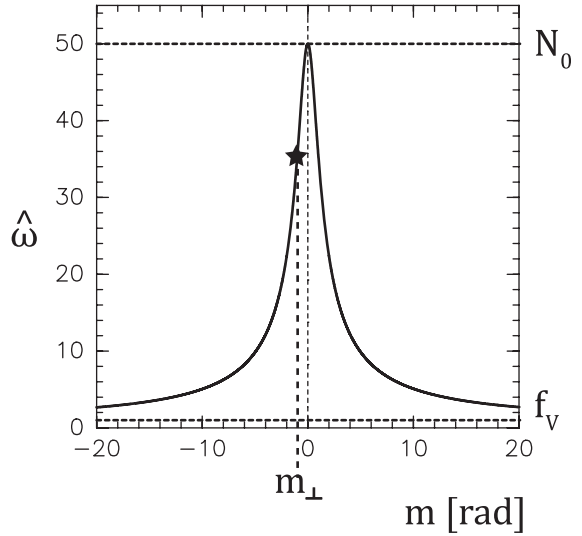


Fig. 12. Frequency $\hat{\omega}$ normalized by f_V as a function of the vertical wave number m normalized by \tilde{k} for $f_H \neq 0$ and $\alpha = \pi/2$. A star on the solid curve denotes the position of m_{\perp} , for which \mathbf{k} is perpendicular to $\mathbf{\Omega}$. $\phi = 45^\circ$ and $N_0 = 50 f_V$ are taken.

(Gerkema and Shrira 2005a; Gerkema and Exarchou 2008).

2. For $f_H = 0$, the hodograph is elliptic and rotates clockwise with time. However, for $f_H \neq 0$, the rotational direction is anticlockwise when m ranges from 0 to m_{\perp} . Here m_{\perp} is the vertical wave number for which $\mathbf{k} \perp \mathbf{\Omega}$. The hodograph becomes linear at $m = m_{\perp}$ in addition to $m = 0$.
3. For $f_H = 0$, the sign of the vertical component of the group velocity is different from that of the vertical phase speed for all internal and equatorial waves. This relation is understood from the form stress over the Θ surface. However, for $f_H \neq 0$, these signs can be the same for the inertia-gravity waves. This is because the f_H -effect can reverse the direction of the form stress through the vertical force balance.
4. The minimum frequency is the increasing function of N_0 for $f_H \neq 0$. This is necessary for the existence of trapped waves in the WSL.
5. The analytic solution trapped in the WSL with a form of a square well for N always has a positive inclination of the phase lines with respect to the y axis regardless of the sign of the meridional wavenumber. This is due to the horizontal anisotropy of the f_H -effect. The trapped wave has a fine vertical structure (the vertical wavelength is

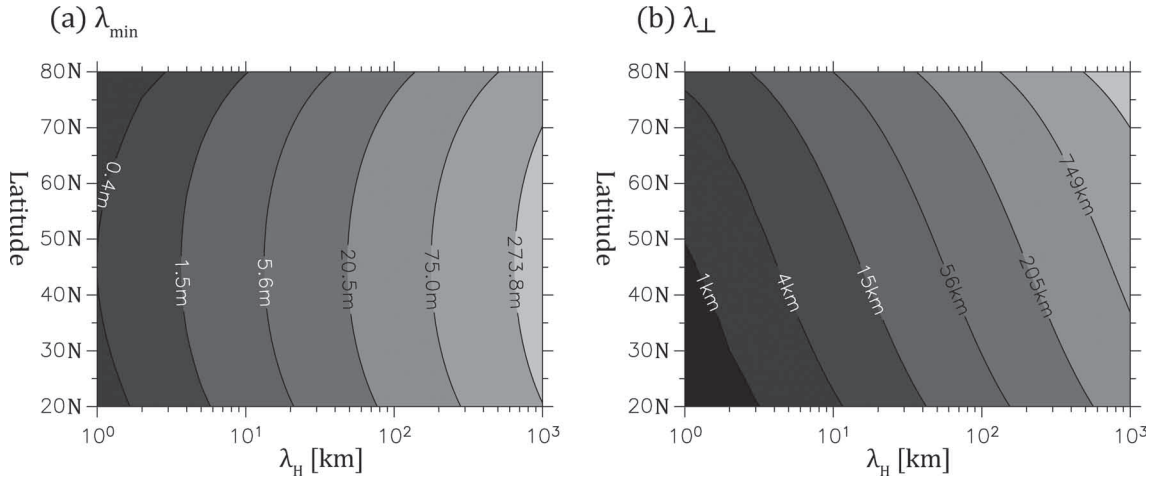


Fig. 13. (a) $\lambda_{\min} \equiv 2\pi/m_{\min}$ as a function of the horizontal wavelength λ_H and latitude for $\alpha = 90^\circ$ and $N_0 = 0.005 \text{ s}^{-1}$. (b) $\lambda_{\perp} \equiv 2\pi/m_{\perp}$ as a function of λ_H and latitude for $\alpha = 90^\circ$. Note that λ_{\perp} does not depend on N_0 .

approximately 1 km) in normal atmospheric conditions.

From analysis of operational radiosonde data in Japan, it was shown that there is a persistent WSL slightly below the tropopause. The possible minimum value of the background N in the WSL (N_{\min}) was $50 f_v$ ($\approx 0.005 \text{ s}^{-1}$), which is about a half times lower than a typical tropospheric value ($\sim 100 f_v$). Using the N_{\min} value, the degree of modification of the hodograph by the f_H -effect and the possibility of the presence of the trapped inertia-gravity waves were examined. The modification of the hodograph would be important when the horizontal wavelength is approximately 100 km and the vertical one is approximately 100 m, for example. As the f_H -effect increases as N decreases, it is necessary to examine the magnitude of N for the hodograph analysis. By using the scale analysis of c_{gz} , it was shown that the condition of $N_{\min} < 0.001 \text{ s}^{-1}$ ($\approx 10 f_v$) is necessary to form a trapped wave within a few days, whose wavelength is in a realistic range. Thus, such trapped waves are rarely observed in the WSL, slightly below the tropopause.

It is well known that wave-like structures are frequently observed near the tropopause (sometimes called tropopausal waves). Their frequencies are low and close to the inertial frequency, and their vertical wavelengths are only a few kilometers (Sato and Woodman 1982; Cornish et al. 1989; Sato and Dunkerton 2002). Such tropopausal waves can play an essential role in the exchange between the troposphere and stratosphere (Danielsen et al. 1991). However, the mechanism of the persistence of such tropopausal

waves is not clear. As there is a persistent WSL slightly below the tropopause, the f_H -effect might facilitate the persistence of such wave disturbances as well as the background shear and/or beta effects. In the mid-latitudes, the typical magnitude of the f_H -term ($f_H W$) is smaller than those of the vertical background shear ($w \frac{dU}{dz}$) and beta ($\beta y v$) terms in the equations of motion by only one or two orders, where U is the zonal component of the background velocity and β is $\frac{df_v}{dy}$. At the equator where f_H is maximized, the magnitude of the f_H -term can be comparable to that of the vertical background shear term in the equations of motion. Thus, the f_H -effect might modify the properties of the equations of motion.

In this paper, to focus on the f_H -effect, we ignored the effect of the latitudinal gradient of f_v (beta effect). Kasahara and Gary (2010) showed that the super-inertial and sub-inertial modes are not largely affected by the beta effect. In particular, the beta effect may be important for the trapped waves at the equator, where f_v is zero, and hence, $\hat{\omega}_{\min}$ is zero (2.11), indicating that the trapped solution does not exist in the linearized Boussinesq model. Moreover, in the ocean, Since the beta effect plays an important role on the transition from the super-inertial to the sub-inertial mode near the critical latitude, wave energy is accumulated in the bottom WSL by the reflection between the bottom surface and the upper SSL (Gerkema and Shrira 2005b). In the atmosphere, an interesting phenomenon may be also present near the critical latitude, which will be studied in the future.

Acknowledgements

We are deeply grateful to Dr. Horinouchi and reviewers for critically reading our manuscript and giving constructive comments. All figures in this paper were produced by GFD-DENNOU Library. This study is supported by a Grant-in-Aid for Scientific Research (B) 22340134 from the Ministry of Education, Culture, Sports, Science and Technology (MEXT), Japan. This manuscript was proofread by a proofreading/editing assistant from the Global COE program. The authors would like to thank Enago (<http://www.enago.jp/>) for the English language review.

Appendix: Exact values of $\hat{\omega}_{\min}$ and $\hat{\omega}_{\max}$

The exact values of $\hat{\omega}_{\min}$ and $\hat{\omega}_{\max}$ are derived using a quadratic form. By substituting (2.7a) into (2.9), the dispersion relation in the $x''y''z''$ coordinates is expressed as

$$\hat{\omega}^2 = (f_V \sin \beta + f_{H\alpha} \cos \beta)^2 + N_0^2 \cos^2 \beta. \quad (\text{A.1})$$

As $\hat{\omega}$ satisfies $\hat{\omega} \neq 0, \infty$, s can be defined as $s \equiv 1/\hat{\omega}$. Further, we, respectively, define q and r as

$$q \equiv s \cos \beta, r \equiv s \sin \beta. \quad (\text{A.2})$$

By substituting (A.2) into (A.1), we obtain

$$1 = \begin{pmatrix} q & r \end{pmatrix} \begin{pmatrix} N_0^2 + f_V^2 + f_{H\alpha}^2 & f_V f_{H\alpha} \\ f_V f_{H\alpha} & f_V^2 \end{pmatrix} \begin{pmatrix} q \\ r \end{pmatrix}. \quad (\text{A.3})$$

Note that (A.3) is a quadratic form expressing an ellipse. The middle matrix is a symmetric matrix; thus, it can be transformed into the diagonal form:

$$1 = \begin{pmatrix} q' & r' \end{pmatrix} \begin{pmatrix} \hat{\omega}_{\max}^2 & 0 \\ 0 & \hat{\omega}_{\min}^2 \end{pmatrix} \begin{pmatrix} q' \\ r' \end{pmatrix}. \quad (\text{A.4})$$

This transformation is equivalent to the rotation of the qr coordinates by an angle γ (Fig. 14). Thus, $\hat{\omega}_{\max}^2$, $\hat{\omega}_{\min}^2$ and γ are, respectively, obtained as follows:

$$\hat{\omega}_{\max, \min}^2 = \frac{N_0^2 + f_V^2 + f_{H\alpha}^2 \pm \sqrt{(N_0^2 + f_V^2 + f_{H\alpha}^2)^2 - 4N_0^2 f_V^2}}{2}, \quad (\text{A.5})$$

$$\gamma = \tan^{-1} \left(\frac{2f_{H\alpha}f_V}{(N_0^2 + f_{H\alpha}^2 - f_V^2) \sqrt{(N_0^2 + f_{H\alpha}^2 - f_V^2)^2 + 4f_{H\alpha}^2 f_V^2}} \right). \quad (\text{A.6})$$

Gerkema and Exarchou (2008) noted that $\hat{\omega}_{\min} < f_V$ and $N_0 < \hat{\omega}_{\max}$ without showing details. This characteristic

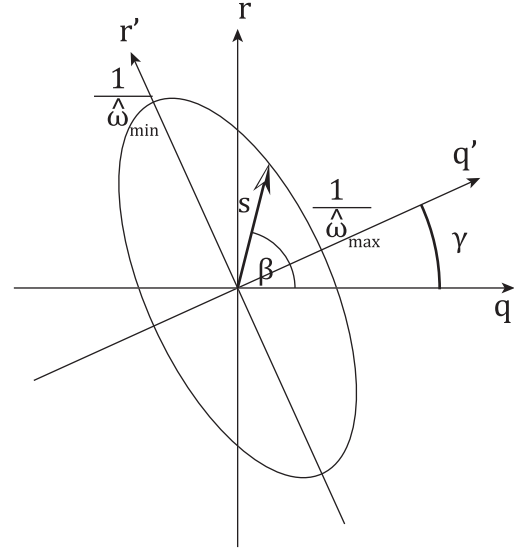


Fig. 14. Ellipse showing the dispersion relation of inertia-gravity waves in the space of $q \equiv \frac{1}{\hat{\omega}} \cos \beta$ and $r \equiv \frac{1}{\hat{\omega}} \sin \beta$. The $q'r'$ coordinates are the principal axes of the dispersion curve. γ is the angle between the q and q' axes, which is given as in (2.14).

is easily understood by writing (A.5) as

$$\hat{\omega}_{\max, \min}^2 = \frac{N_0^2 + f_V^2 + f_{H\alpha}^2 \pm \sqrt{(N_0^2 - f_V^2 + f_{H\alpha}^2)^2 + 4N_0^2 f_V^2}}{2}, \quad (\text{A.7})$$

and by using

$$(N_0^2 - f_V^2 + f_{H\alpha}^2)^2 < \sqrt{(N_0^2 - f_V^2 + f_{H\alpha}^2)^2 + 4f_{H\alpha}^2 f_V^2}.$$

References

- Andrews, D. G., J. R. Holton, and C. B. Leovy, 1987: Middle atmosphere dynamics. *Academic Press*, 489 pp.
- Cornish, C. R., and M. F. Larsen, 1989: Observations of low-frequency inertia-gravity waves in the lower stratosphere over Arecibo. *J. Atmos. Sci.*, **46**, 2428–2439.
- Danielsen, E. F., R. S. Hipskind, W. L. Starr, J. F. Vedder, S. E. Gaines, D. Kley, and K. K. Kelly, 1991: Irreversible transport in the stratosphere by internal waves of short vertical wavelength. *J. Geophys. Res.*, **96**, 17433–17452.
- Durrant, D. R., and C. Bretherton, 2004: Comments on “the roles of the horizontal component of the Earth’s angular velocity in nonhydrostatic linear models”. *J. Atmos. Sci.*, **61**, 1982–1986.
- Gerkema, T., and E. Exarchou, 2008: Internal-wave properties in weakly stratified layers. *J. Mar. Res.*, **66**, 617–644.
- Gerkema, T., and V. I. Shrira, 2005a: Near-inertial waves in the ocean: Beyond the ‘traditional approximation’. *J.*

- Fluid Mech.*, **529**, 195–219.
- Gerkema, T., and V. I. Shrira, 2005b: Near-inertial waves on the “nontraditional” β plane. *J. Geophys. Res.*, **110**, CO1003, doi:10.1029/2004JC002519.
- Holton, J. R., 2004: An introduction to dynamic meteorology. *Elsevier Academic Press*, 535 pp.
- Japan Meteorological Agency, 1995: Guideline for Aerological Observation. *Japan Meteorological Agency*, 153 pp.
- Kasahara, A., 2003: The roles of the horizontal component of the Earth’s angular velocity in nonhydrostatic linear models. *J. Atmos. Sci.*, **15**, 1085–1095.
- Kasahara, A., and J. M. Gary, 2006: Normal modes of an incompressible and stratified fluid model including the vertical and horizontal components of Coriolis force. *Tellus*, **58A**, 368–384.
- Kasahara, A., and J. M. Gary, 2010: Studies of inertio-gravity waves on midlatitude betaplane without the traditional approximation. *Quart. J. Roy. Meteor. Soc.*, **136**, 517–536.
- Pedlosky, J., 1987: Geophysical fluid dynamics. *Springer-Verlag New York Inc.*, 710 pp.
- Saint-Guilly, B., 1970: On internal waves: Effects of the horizontal component of the Earth’s rotation and of a uniform current. *Dtsch. Hydrogr. Z.*, **23**, 16–23.
- Sato, K., 1994: A statistical study of the structure, saturation and sources of inertio-gravity waves in the lower stratosphere observed with the MU radar. *J. Atmos. Terr. Phys.*, **56**, 755–774.
- Sato, K., and T. J. Dunkerton, 2002: Layered structure associated with low potential vorticity near the tropopause seen in high-resolution radiosondes over Japan. *J. Atmos. Sci.*, **59**, 2782–2800.
- Sato, T., and R. F. Woodman, 1982: Fine altitude resolution radar observations of upper-tropospheric and lower-stratospheric winds and waves. *J. Atmos. Sci.*, **39**, 2539–2545.
- Thuburn, J., N. Wood, and A. Staniforth, 2002: Normal modes of deep atmospheres. II: f - F plane geometry. *Quart. J. Roy. Meteor. Soc.*, **128**, 1793–1806.
- Vallis, G. K., 2006: Atmospheric and oceanic fluid dynamics: Fundamentals and large-scale circulation. *Cambridge University Press*, 745 pp.
- White, A. A., B. J. Hoskins, I. Roulstone, and A. Staniforth, 2005: Consistent approximate models of the global atmosphere: Shallow, deep, hydrostatic, quasi-hydrostatic and non-hydrostatic. *Quart. J. Roy. Meteor. Soc.*, **131**, 2081–2107.